

# MEDTRINITY-25M: A LARGE-SCALE MULTIMODAL DATASET WITH MULTIGRANULAR ANNOTATIONS FOR MEDICINE

**Anonymous authors**

Paper under double-blind review

## ABSTRACT

This paper introduces MedTrinity-25M, a comprehensive, large-scale multimodal dataset for medicine, covering over 25 million images across 10 modalities, with multigranular annotations for more than 65 diseases. These multigranular annotations encompass both global information, such as modality and organ detection, and local information like ROI analysis, lesion texture, and region-wise correlations. Unlike the existing multimodal datasets, which are limited by the availability of image-text pairs, we have developed the first automated pipeline that scales up multimodal data by generating multigranular visual and textual annotations in the form of image-ROI-description triplets without the need for any paired text descriptions. Specifically, data from over 30 different sources have been collected, preprocessed, and grounded using domain-specific expert models to identify ROIs related to abnormal regions. We then build a comprehensive knowledge base and prompt multimodal large language models to perform retrieval-augmented generation with the identified ROIs as guidance, resulting in multigranular textual descriptions. Compared to existing datasets, MedTrinity-25M provides the most enriched annotations, supporting a comprehensive range of multimodal tasks such as captioning and report generation, as well as vision-centric tasks like classification and segmentation. We propose LLaVA-Tri by pretraining LLaVA on MedTrinity-25M, achieving state-of-the-art performance on VQA-RAD, SLAKE and PathVQA, surpassing representative SOTA multimodal large language models. Furthermore, MedTrinity-25M can also be utilized to support large-scale pre-training of multimodal medical AI models, contributing to the development of future foundation models in the medical domain. We will make our dataset available.

## 1 INTRODUCTION

Large-scale multimodal foundation models (Liu et al., 2024; Achiam et al., 2023; Tu et al., 2024b; Team et al., 2023b; Zhou et al., 2024) have demonstrated remarkable success across various domains due to their ability to understand complex visual patterns in conjunction with natural language. This success has sparked significant interest in applying such models to medical vision-language tasks. Much progress has been made to improve the medical capacity of general domain multimodal foundation models by constructing medical datasets with image-text pairs and fine-tuning general domain models on these datasets (Bustos et al., 2020; Irvin et al., 2019; Johnson et al., 2019a; Li et al., 2024a; Ikezogwo et al., 2024).

However, current medical datasets have several limitations. Firstly, these datasets lack **multigranular** annotations that reveal the correlation between region-wise information within medical images. Medical images often contain detailed cues, such as regional abnormal textures or structures, which may indicate specific types of lesions. Therefore, multimodal models need the ability to infer global information, such as disease

047 or lesion type, from local details. The absence of such data limits the models' capacity to comprehensively  
048 understand medical images. Moreover, current dataset construction methods heavily rely on medical images  
049 paired with reports or captions from human experts (Ikezogwo et al., 2024; Liu et al., 2021; Lau et al., 2018b;  
050 He et al., 2020a), which restricts their scalability.

051 In this paper, we address the above challenges by proposing an automated data construction pipeline us-  
052 ing multimodal large language models (MLLMs) without relying on paired text descriptions. To address  
053 the scarcity of medical knowledge within general-purpose MLLMs, we incorporate retrieval-augmented  
054 generation (RAG) to source relevant medical knowledge from a medical database for MLLMs's reference.  
055 To enhance the model's regional focus, we employ an ensemble of domain-specific segmentation mod-  
056 els and grounding models to generate regions of interest (ROIs). MLLMs are then prompted to produce  
057 multigranular visual and textual annotations, enriched by the retrieved medical knowledge and ROIs. Our  
058 proposed pipeline enables the transformation of large-scale images without paired ROIs or text into image-  
059 ROI-description triplets. These triplets provide multigranular annotations that encompass both global tex-  
060 tual information, such as disease/lesion type, modality, and inter-regional relationships, as well as detailed  
061 local annotations for ROIs, including bounding boxes, segmentation masks, and region-specific textual de-  
062 scriptions. Using the proposed pipeline, we create a large-scale multimodal multigranular medical dataset  
063 containing over 25 million triplets, namely **MedTrinity-25M**. To best of our knowledge, this is the largest  
064 multimodal dataset in medicine to date.

065 To demonstrate the effectiveness of our dataset, we proposed **LLaVA-Tri** by pretraining LLaVA  
066 on MedTrinity-25M. We conduct extensive evaluations across three external medical visual QA datasets  
067 representing different sub-pathologies. LLaVA-Tri achieved state-of-the-art results in all of the three VQA  
068 benchmarks, with 81.6% accuracy on VQA-RAD (Lau et al., 2018b), 87.8% on SLAKE (Liu et al., 2021),  
069 and 82.8% on PathVQA (He et al., 2020a). Moreover, consistent performance improvements are observed  
070 when pretraining other multimodal models on MedTrinity-25M. These findings emphasize the potential of  
071 MedTrinity-25M as a foundational dataset that can improve the medical performance of diverse multimodal  
072 models.

## 073 2 RELATED WORK

074 **Medical Multimodal Foundation Models.** Due to the success of multimodal foundation models in com-  
075 prehending visual features, their adaptation for medical vision-language tasks has garnered increasing atten-  
076 tion (Moor et al., 2023; Tu et al., 2024a; Li et al., 2024a; Zhou et al., 2024). Several works adapt general  
077 multimodal models to the medical domain via end-to-end training on medical datasets. For instance, Med-  
078 Flamingo (Moor et al., 2023) fine-tunes OpenFlamingo-9B (Awadalla et al., 2023) using 0.8M interleaved  
079 and 1.6M paired medical image-text data. LLaVA-Med (Li et al., 2024a) uses a two-stage end-to-end visual  
080 instruction tuning (Liu et al., 2024), excelling in medical visual question answering (VQA) tasks. Med-  
081 Gemini (Saab et al., 2024) adapts Gemini (Team et al., 2023a) using a long-form question answering dataset  
082 to enhance multimodal and long-context capabilities. Despite these achievements, the limited scale of train-  
083 ing data remains a challenge. Prior research (Kaplan et al., 2020) shows that increasing training data size  
084 improves large multimodal model performance. This paper aims to build a large-scale medical dataset to  
085 drive the development of stronger medical multimodal foundation models.

086 **Multimodal Datasets for Medicine.** The importance of constructing medical multimodal datasets has  
087 drawn significant attention (Li et al., 2024a; Pelka et al., 2018; Zhang et al., 2024; Irvin et al., 2019). Sev-  
088 eral works focus on collecting images paired with clinical reports from specialists (Zhang et al., 2024; Irvin  
089 et al., 2019; Johnson et al., 2019a), providing detailed descriptions, including disease types and reasoning.  
090 For instance, MIMIC-CXR (Johnson et al., 2019a) contains 227,835 images for 65,379 patients, with cor-  
091 responding reports. However, constructing such reports manually is time-consuming and costly, limiting  
092 dataset size. PMC-OA (Lin et al., 2023) includes up to 1.65 million image-caption pairs from medical pa-  
093

pers but lacks detailed clinical reports. RadGenome-Chest CT (Zhang et al., 2024) offers richer annotations but remains dependent on paired image-text data, limiting its scale. In comparison, we introduce the first automated pipeline to generate multigranular annotations for independent images, generating a comprehensive dataset containing 25 million samples.

### 3 MEDTRINITY-25M DATASET

#### 3.1 DATA TRIPLET

In this section, we provide details about data format within MedTrinity-25M. Our dataset comprises triplets of  $\{\text{image}, \text{ROI}, \text{description}\}$ . For each image, we provide multigranular annotations containing both textual description and visual ROI.

**Images.** We gather 25,016,845 samples across 10 medical image modalities and over 65 diseases. Specifically, we utilize original medical images from various datasets, extensively collecting from online sources such as TCIA, Kaggle, Zenodo, Synapse, Hugging Face, Grand Challenge, GitHub, and medical datasets including CheXpert (Irvin et al., 2019) and DeepLesion (Yan et al., 2017a). 3D volumetric images in DICOM or NIfTI formats are converted to 2D slices with PNG format. The detailed data sources are illustrated in Appendix A.

**ROIs.** We use ROIs to provide visual annotations for each image, primarily focusing on pathological findings such as lesions, inflammation, neoplasms, infections, and other abnormalities. In cases without such abnormalities, the ROIs generally mark the primary object or organ in the image, as illustrated in Figure 10. When multiple organs are relevant for disease diagnosis, the ROIs aim to cover several regions associated with the disease, providing detailed analysis of each affected area, as shown in Figure 11.

**Textual Descriptions.** The textual descriptions for each image are composed of detailed information across various attributes. In contrast to the unstructured medical reports or short captions in previous medical datasets (Irvin et al., 2019; Johnson et al., 2019a; Bustos et al., 2020; Zhang et al., 2023b; Liu et al., 2021; Pelka et al., 2018; Lin, 2023), our textual descriptions are structured and contain multigranular information for five attributes. As illustrated in Figure 1, the general attributes of the image are described initially, covering aspects such as modality, the detection of specific organs, and their depiction. Following this, the attributes related to ROI are detailed, including the ROI analysis, locations and texture of the lesions, which encompass the disease type and relevant pathological features. Furthermore, region-wise correlations are highlighted to showcase relationships between the ROIs and surrounding regions, providing insight into differences in features and the extent of disease progression.

#### 3.2 DATA CONSTRUCTION PIPELINE

Given a medical image, we aim to generate corresponding multigranular visual and textual annotations. Specifically, as shown in Figure 2, our pipeline can be decomposed into two stages: 1) *Data Processing*, and 2) *Multigranular Textual Description Generation*. Firstly, our data processing stage includes three key steps: a) *Metadata Integration* to produce coarse captions encapsulating fundamental image information such as modality and disease types; b) *ROI Locating* to identify regions of abnormalities; and c) *Medical Knowledge Retrieval* to extract relevant fine-grained medical details. All processing steps are further detailed in Section 3.2.1. Subsequently, we prompt MLLMs to integrate information within processed data and generate multigranular textual descriptions. Corresponding details are provided in Section 3.2.2. The original image, generated visual ROIs and textual descriptions are combined into a data triplet in MedTrinity-25M.

141  
142  
143  
144  
145  
146  
147  
148  
149  
150  
151  
152  
153  
154  
155  
156  
157  
158  
159  
160  
161  
162  
163  
164  
165  
166  
167  
168  
169  
170  
171  
172  
173  
174  
175  
176  
177  
178  
179  
180  
181  
182  
183  
184  
185  
186  
187

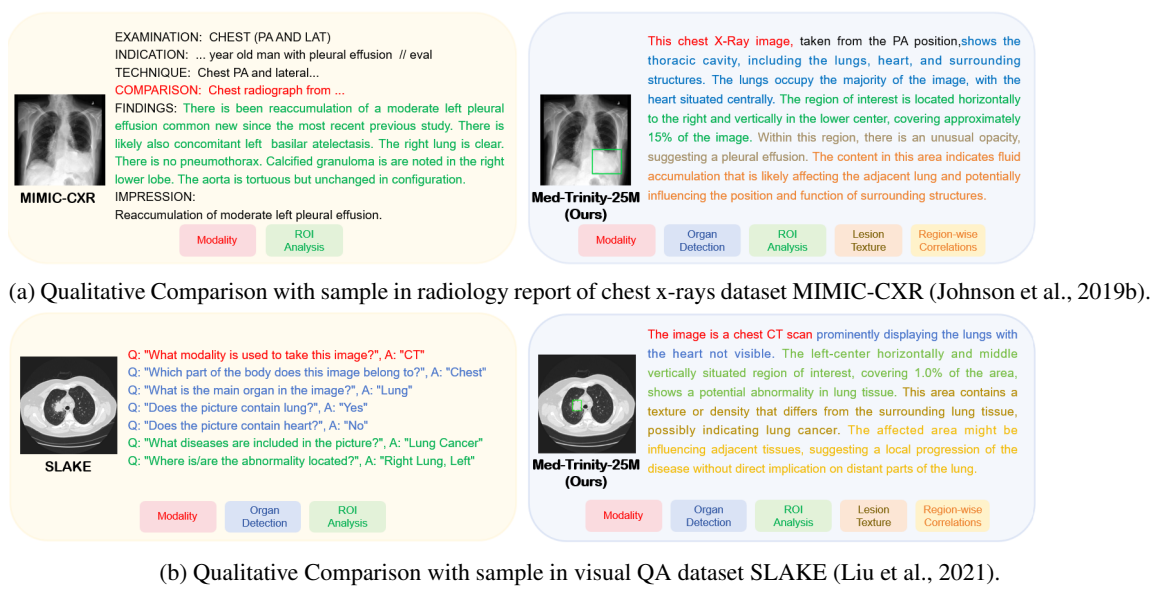


Figure 1: Qualitative comparison with different types of dataset.

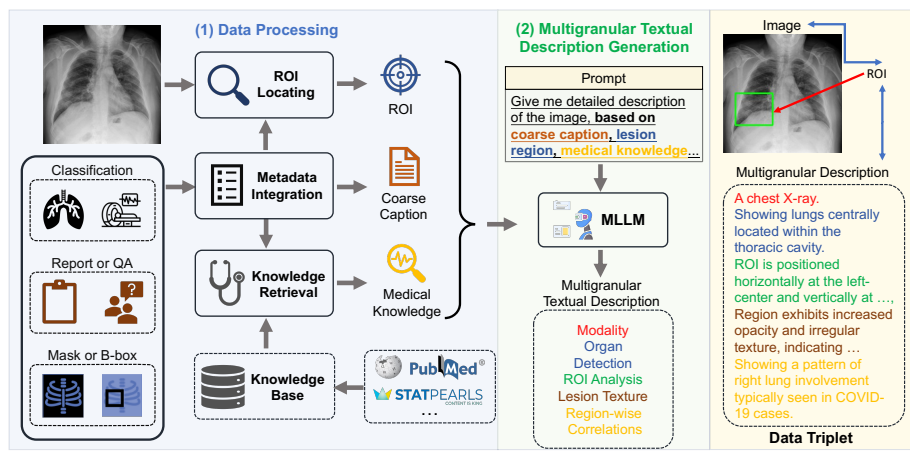


Figure 2: **Data construction pipeline.** 1) *Data processing*, including metadata integration to generate coarse caption, ROI locating, and medical knowledge collection. 2) *Multigranular Textual Description Generation* based on processed data.

### 3.2.1 DATA PROCESSING

**Coarse Caption Generation via Metadata Integration.** We aim to generate coarse captions that provide fundamental information for a given image, including modality, organ labels, disease types, and optionally, camera views and equipment information. Instead of extracting features directly from the images, we generate these captions by integrating dataset metadata. We first extract metadata from the datasets and then apply a fixed rule to integrate this information into coarse captions. For example, for an image in the QaTa-

188  
189  
190  
191  
192  
193  
194  
195  
196  
197  
198  
199  
200  
201  
202  
203  
204  
205  
206  
207  
208  
209  
210  
211  
212  
213  
214  
215  
216  
217  
218  
219  
220  
221  
222  
223  
224  
225  
226  
227  
228  
229  
230  
231  
232  
233  
234

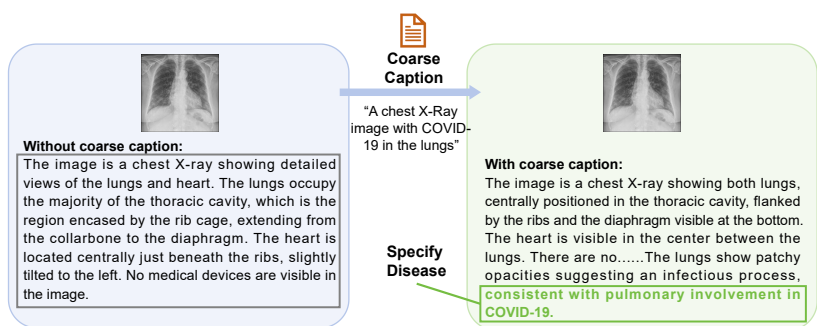


Figure 3: A qualitative comparison example of generated textual description with and without coarse caption. Without a coarse caption, MLLMs fails to detect diseases. On the contrary, providing a caption mentioning “COVID-19” allows MLLMs to identify and categorize the disease, facilitating further analysis.

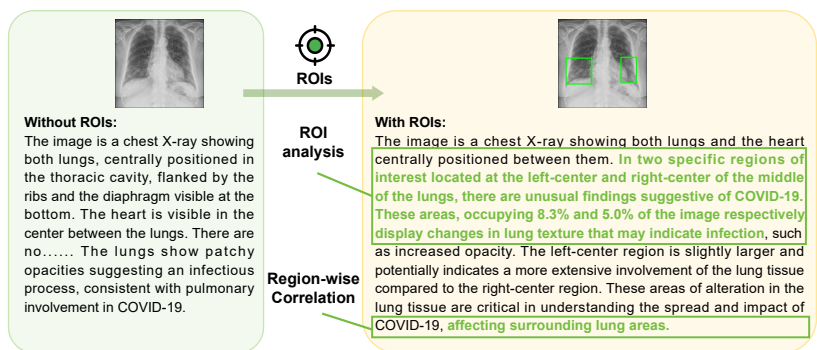


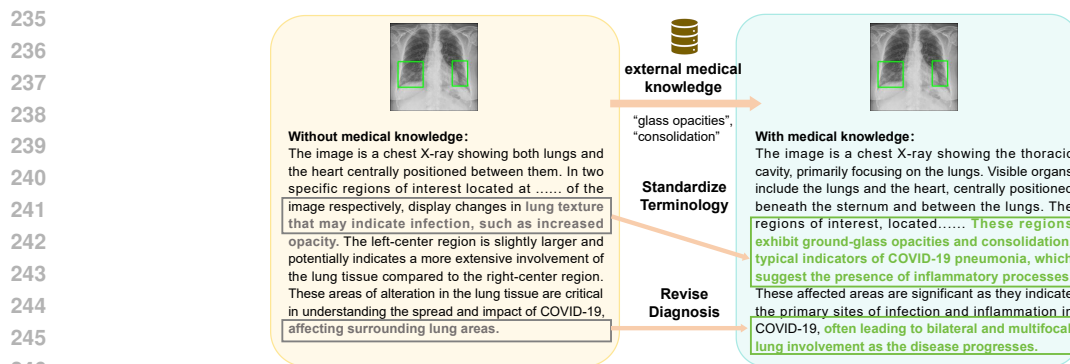
Figure 4: A qualitative comparison example of generated textual description with and without locating ROIs. Without ROIs, the caption offers only a brief global analysis; with ROIs, MLLMs conducts detailed local analysis and assesses the impact of lesion ROIs on adjacent normal regions.

COVID-19 dataset<sup>1</sup>, we derive metadata from the dataset’s accompanying paper or documentation, indicating that it consists of COVID-19 chest X-ray images. Next, we construct coarse captions like “A chest X-ray image with COVID-19 in the lungs” highlighting the modality, organ types, and disease labels. We also integrate additional paired textual information (if any), such as radiological findings into coarse captions.

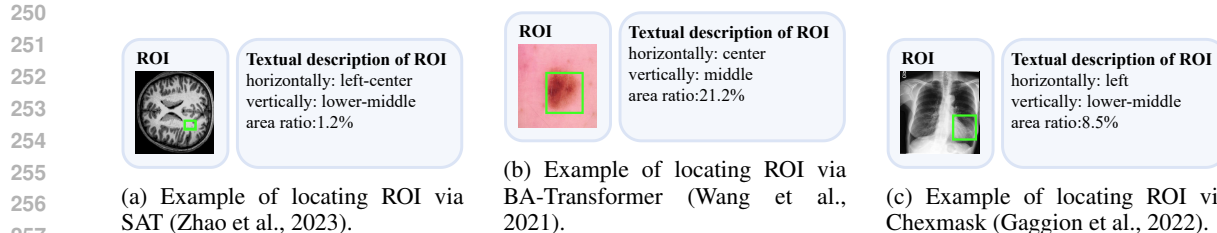
The effectiveness of applying coarse captions when generating multigranular textual descriptions is illustrated in Figure 3. In contrast to the scenario without a coarse caption, where MLLMs fails to recognize the disease, providing MLLMs with a coarse caption that includes the disease type “COVID-19” enables it to identify and categorize the disease, thereby laying the foundation for further analysis.

**ROI Locating.** We employ appropriate strategies to locate ROIs for images paired with different annotations. For datasets that already include localization annotations, such as segmentation masks or bounding boxes, we derive the ROIs from these paired annotations. Specifically, bounding boxes are directly used as the ROIs, while segmentation masks are converted to ROIs by creating the smallest bounding box that covers the mask. When such localization annotations are not available, we apply corresponding pretrained expert models to generate ROIs. More details about the selection of expert models are provided in Appendix D. Examples of generated ROIs from various modalities using corresponding models are demonstrated in Fig-

<sup>1</sup><https://www.kaggle.com/aysendegerli/qatacov19-dataset>.



247 **Figure 5: A qualitative comparison example of generated textual description with and without external**  
248 **medical knowledge.** MLLMs can standardize medical terminology in its expressions and refine its diagnosis  
249 based on disease progressions detailed in medical literature.



258 **Figure 6: Example of ROIs and their corresponding textual descriptions.**

260 ure 6. For modalities such as X-ray and MRI scans viewed from the z-axis, our ROI localization employs a  
261 coordinate system relative to the human body, resulting in a left-right reversal in the image representation.

262 Incorporating ROIs as the guidance facilitates MLLMs to conduct a detailed analysis and generate multi-  
263 granular textual descriptions. As demonstrated in Figure 4, description generated without guidance of ROIs  
264 is limited to a brief global overview of the image. In comparison, with ROIs, generated description contains  
265 local analysis regarding the abnormal region and its correlations to other regions.

267 **Medical Knowledge Retrieval.** General-purpose MLLMs often lacks medical terminology and expertise.  
268 To address this issue, we build a medical knowledge database following MedRAG (Xiong et al., 2024). We  
269 collect three main corpora: PubMed<sup>2</sup> for biomedical knowledge, StatPearls<sup>3</sup> for clinical decision support,  
270 and medical textbooks (Jin et al., 2021) for domain-specific knowledge. We segment these corpora into short  
271 snippets and encode them into high-dimensional vectors using the text encoder from Med-CPT (Jin et al.,  
272 2023). These vectors are then indexed into a specialized vector knowledge base using Faiss(Johnson et al.,  
273 2019c), optimized for efficient retrieval. For a given image, we retrieve relevant medical knowledge by us-  
274 ing its coarse caption, which is generated through metadata integration. Specifically, we encode the coarse  
275 captions, including disease and organ classifications, into vectors using the Med-CPT text encoder. We then  
276 perform a vector similarity search in the medical vector database, retrieving the top eight medical knowledge  
277 snippets that semantically match the query. These snippets provide the external medical knowledge paired  
278 with the image for generating textual descriptions. A qualitative example demonstrating the effectiveness  
279 of incorporating external medical knowledge is shown in Figure 7. With access to COVID-19-related med-

280 <sup>2</sup><https://pubmed.ncbi.nlm.nih.gov/>

281 <sup>3</sup><https://www.statpearls.com/>

282 **Knowledge 1:**  
 283 **Title: Mobile chest X-ray manifestations of 54 deceased patients with coronavirus disease 2019: Retrospective study.**  
 284 Content: ..... We found that 50 (93%) patients with **lesions occurred in the bilateral lung**, 4 (7%) patients occurred in the right lung, 54 (100%)  
 285 patients were **multifocal involvement**. The number of lung fields involved was 42 (78%) patients in 6 fields, 3 (6%) patients in 5 lung fields, 4  
 286 (7%) patients in 4 lung fields, and 5 (9%) patients in 3 lung fields. Fifty-three (98%) patients had **patchy opacities**, 3 (6%) patients had round or  
 287 **oval solid nodules**, 9 (17%) patients had fibrous stripes, 13 (24%) patients had **pleural effusion**, 8 (15%) patients had **pleural thickening**, 6  
 288 (11%) patients had **pneumothorax**, 3 (6%) patients had **subcutaneous emphysema**. Among the 24 patients who had serial mobile chest X-rays,  
 16 (67%) patients had the progression of the lesions, 8 (33%) patients had no significant change of the lesions, and there was no case of  
 289 reduction of the lesions. The mobile chest X-ray manifestations of deceased patients with COVID-19 were **mostly bilateral lung, multifocal  
 involvement, and extensive lung field, and pleural effusion, pleural thickening, and pneumothorax probably could be observed**. The  
 serial mobile chest X-ray showed that the chest lesions were progressive with a high probability.  
 .....

290 Figure 7: **An example of the Top-8 retrieval results.** By leveraging COVID-19-related medical knowledge,  
 291 MLLMs can standardize medical terminology and enhance diagnoses according to the disease progressions  
 292 described in medical literature.

294 ical knowledge, MLLMs can standardize medical terminology and refine diagnoses based on the disease  
 295 progressions outlined in medical literature.

296 A qualitative comparison of generated text descriptions, both with and without external medical knowl-  
 297 edge, is presented in Figure 5. MLLMs are capable of standardizing medical terminology and enhancing  
 298 diagnostic accuracy by incorporating insights from disease progressions documented in medical literature.

### 300 3.2.2 GENERATION OF MULTIGRANULAR TEXT DESCRIPTION

302 **Generation Prompt.** After data processing, a comprehensive prompt is utilized to guide MLLMs to in-  
 303 tegrate all information and generate multi-granular descriptions. We incorporate the processed data (coarse  
 304 captions, ROIs, and retrieved medical knowledge) into the prompts. Specifically, textual information such  
 305 as coarse captions and retrieved medical knowledge are directly integrated into the prompt. While ROIs on  
 306 images are converted into textual information based on their coordinates and area ratio within the images,  
 307 using terms such as “left-center” and “area ratio: 1.2%”. Examples of textual information converted from  
 308 ROIs are shown in Figure 6. Instead of merely inserting retrieved knowledge, we instruct MLLM to identify  
 309 and align the relevant knowledge with ROIs to provide diagnostic insights. The prompt template consists of  
 310 a three-level hierarchical framework with questions to instruct MLLMs to generate: (1) a global descrip-  
 311 tion that captures all details of the image, (2) a local-focused analysis of specific ROIs that potentially are  
 312 diseased; and (3) an inference of the correlations between region-wise attributes to understand the impact of  
 313 local abnormalities on the surrounding regions and extent of disease progression. Detailed prompt template  
 314 is presented in Appendix F.

315 **Choice of MLLM.** All textual description in MedTrinity-25M are generated using LLaVA-Medcap, which  
 316 is a specifically fine-tuned LLaVA to generate high-quality textual descriptions. To obtain the fine-tuning  
 317 data, we first generate 200,000 multigranular textual descriptions using our generation pipeline and GPT-  
 318 4V (Achiam et al., 2023). Subsequently, we pretrain our LLaVA-Medcap following the two-stage fine-tuning  
 319 strategy in LLaVA-Med (Li et al., 2024a), then these generated data are used to to finetune the LLaVA-  
 320 Medcap. LLaVA-Medcap is then used in our pipeline to generate text descriptions for whole 25 million  
 321 images in MedTrinity-25M. As shown in Appendix B, LLaVA-Medcap is capable of generating high-quality  
 322 descriptions with more details compared to GPT-4V.

### 324 3.3 DATASET ANALYSIS

326 **Scale.** Figure 8c compares the amount of data samples in MedTrinity-25M and other medical multimodal  
 327 datasets. To the best of our knowledge, MedTrinity-25M is the largest open-source, multi-modal multigran-  
 328 ular medical dataset to date.

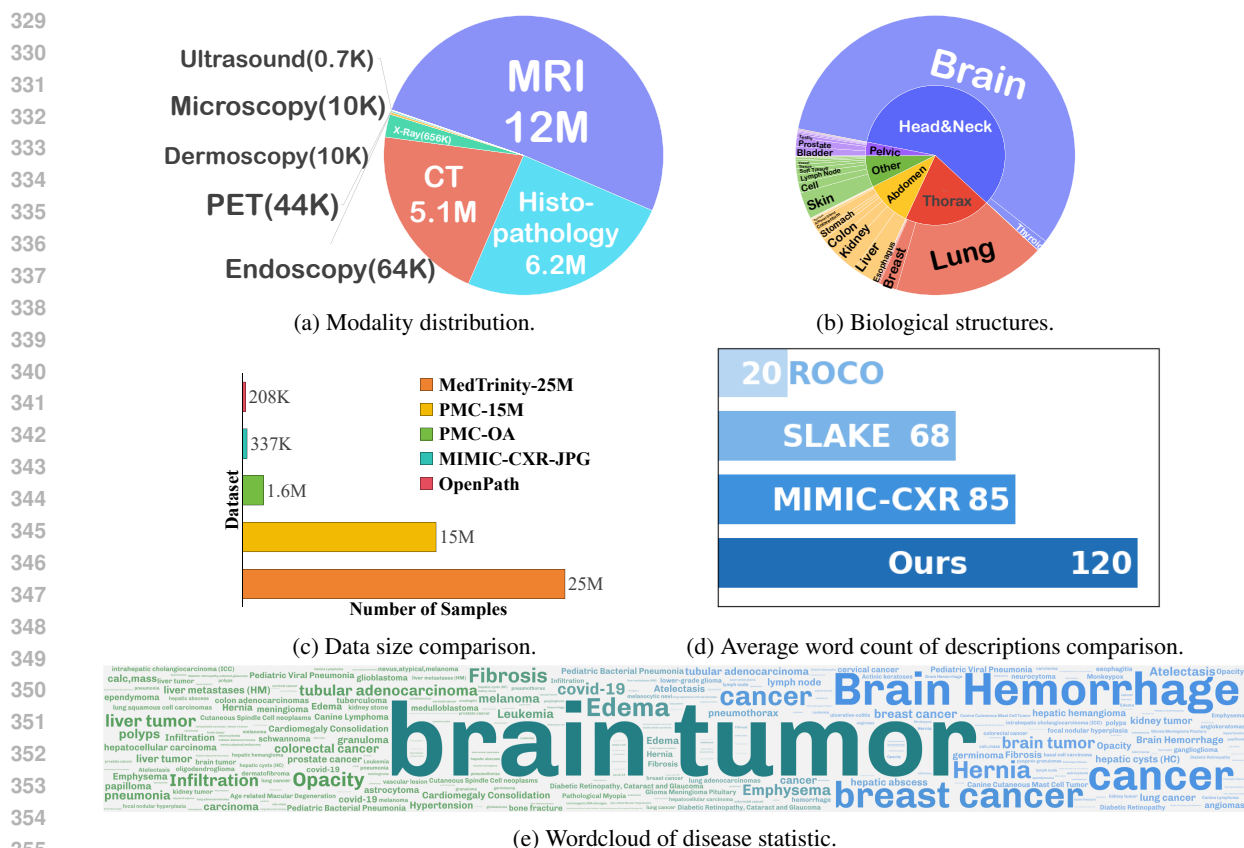


Figure 8: Statistical overview of MedTrinity-25M.

**Diversity.** Our dataset encompasses 10 imaging modalities, with more than 65 diseases across various anatomical structures in human. The number of the samples within each modality in MedTrinity-25M are shown in Figure 8a, and the distribution of each anatomical and biological structures is provided in Figure 8b. Meanwhile, Figure 8e illustrates the frequently used words related to diseases in our dataset.

**Richness.** We provide both qualitative examples and quantitative analysis to demonstrate the richness of annotations in MedTrinity-25M. As shown in Table 1, we compare the types of annotations in our dataset with those of other multimodal datasets. Our dataset provides multigranular and richer annotation information, surpassing other multimodal datasets. Qualitative examples are shown in Figure 1. Our textual descriptions provide more comprehensive information compared to the chest X-rays dataset MIMIC-CXR (Johnson et al., 2019b) and the visual QA dataset SLAKE (Liu et al., 2021). Figure 8d compares the average word count of text descriptions in multiple medical multimodal datasets. The word count in our dataset is significantly larger, indicating greater richness.

**Quality.** We conduct expert and LLM evaluations to verify the quality of the generated multigranular descriptions. Each description in MedTrinity-25M contains five key attributes of medical images: modality, organ detection, ROI analysis, lesion texture, and region-wise correlations. A random subset of 200 samples is selected for evaluation. In expert-based evaluation, medical professionals assess the accuracy of each attribute by comparing the generated descriptions with ground-truth annotations. Scores are averaged across



Table 1: Comparison of types of annotations in MedTrinity-25M with other multimodal datasets.

Dataset	Modality	Lesion Type	Lesion BBox/Mask	Lesion Description	Region-wise Correlations
MedMNIST (Yang et al., 2023)	✗	✓	✗	✗	✗
DeepLesion (Yan et al., 2017b)	✓	✗	✓	✗	✗
BraTS 2024 (de Verdier et al., 2024a)	✓	✗	✓	✗	✗
MIMIC-CXR (Johnson et al., 2019b)	✓	✓	✓	✓	✗
Quilt-1M (Ikezogwo et al., 2024)	✓	✓	✗	✓	✓
VQA-RAD (Lau et al., 2018a)	✓	✓	✗	✓	✗
CRC100K (Kather et al., 2018)	✓	✓	✗	✗	✗
SA-Med2D-20M (Ye et al., 2023)	✓	✓	✓	✗	✗
<b>MedTrinity-25M(Ours)</b>	✓	✓	✓	✓	✓

Table 2: Comparison of alignment scores between LLM and Expert.

Evaluator	Attributes					Avg.
	Modality	Organ Detection	ROI Analysis	Lesion Texture	Region-wise Correlations	
LLM	1.00/1.00	0.90/1.00	0.90/1.00	0.80/1.00	0.70/1.00	0.86/1.00
Expert	1.00/1.00	0.90/1.00	0.90/1.00	0.70/1.00	0.80/1.00	0.85/1.00

all samples to obtain an overall score. For LLM-based evaluation, we use GPT-4V to assess the accuracy of medical facts and diagnoses based on the same five attributes. GPT-4V scores each attribute on a scale of 0 to 2 points. All scores are normalized to a 0–1 scale for comparison.

Table 2 shows that MedTrinity-25M achieves 0.85 and 0.86 in expert and LLM evaluations, with modality, organ detection, and ROI analysis nearing perfect scores. To illustrate, Figure 12 shows a sample that achieved a perfect score from GPT-4V.

## 4 EXPERIMENT

### 4.1 LLaVA-TRI: ALIGNING MULTISCALE MLLM WITH MEDTRINITY-25M

To fully exploit the multigranular annotations, we propose LLaVA-Tri, which is based on LLaVA (Liu et al., 2024) and incorporate MedTrinity-25M to align it into medical domain. LLaVA-Tri integrates LLaMA3 (Team, 2024) to enhance linguistic capabilities and incorporates multiscale feature extraction (Shi et al., 2024) to boost visual performance. Specifically, we firstly pretrain LLaVA-Tri on 600K image-text pairs from PMC-15M (Zhang et al., 2023a), following the training settings from Li et al. (2024a). The model is then trained on MedTrinity-25M for multigranular alignment. We benchmark LLaVA-Tri on three biomedical Visual Question Answering (VQA) datasets, VQA-RAD (Lau et al., 2018a), SLAKE (Liu et al., 2021), and PathVQA (He et al., 2020a), to assess the efficacy of aligning model using MedTrinity-25M. The model is fine-tuned for three epochs on each of the three VQA datasets and evaluate accordingly.

As shown in Table 3, LLaVA-Tri achieved state-of-the-art results in all of the three VQA benchmarks, with 81.6% accuracy on VQA-RAD, 87.8% on SLAKE, and 82.8% on PathVQA. These results highlight the significant advantages of incorporating multiscale LLaVA-Tri with multigranular alignment.

### 4.2 ENHANCING MODEL PERFORMANCE THROUGH MULTIGRANULAR ALIGNMENT

To further demonstrate the effectiveness of multigranular alignment, we conducted ablation studies by training and evaluating model with or without aligning using MedTrinity-25M respectively. We conduct experiment on various multimodal models, including both multimodal language models and CLIP models:

Table 3: **Comparison of LLaVA-Tri with Existing SOTA Methods.** LLaVA-Tri achieves SOTA performance on all three VQA benchmarks by employing multigranular alignment pretraining on MedTrinity-25M. The asterisk (\*) indicates that, for open-ended questions, prior methods formulate the problem as classification among distinct answers in the training set, potentially overestimating generalizability. Open: Open-ended questions where the model generates free-form text responses without predefined answer options. Closed: Closed-ended questions where the model selects from a predefined set of possible answers.

Method	VQA-RAD			SLAKE			PathVQA		
	Open	Closed	Avg	Open	Closed	Avg	Open	Closed	Avg
<b>Method Not Finetuned on the Training Set of the VQA Benchmark</b>									
GPT-4V	39.5	78.9	59.2	33.6	43.6	38.6	-	-	-
LLaVA-Med	28.2	61.4	44.8	39.2	52.2	45.7	12.3	54.1	33.2
<b>LLaVA-Tri</b>	<b>36.9</b>	<b>62.6</b>	<b>49.7</b>	<b>24.1</b>	<b>43.4</b>	<b>33.7</b>	<b>11.2</b>	<b>59.0</b>	<b>35.1</b>
<b>Method Finetuned on the Training Set of the VQA Benchmark</b>									
<b>Clip-based</b>									
PubMedCLIP	60.1	80.0	70.1	78.4	82.5	80.5	-	-	-
BiomedCLIP	67.6	79.8	73.7	82.1	89.7	85.9	-	-	-
<b>Non Clip-based</b>									
VL Encoder-Decoder	71.5	82.5	77.0	-	-	-	71.5	85.6	78.6
Q2ATransformer	79.2	81.2	80.2	-	-	-	54.9	88.9	71.9
Prefix T. Medical LM	-	-	-	84.3	82.0	83.2	40.0	87.0	63.5
M2I2	66.5	83.5	75.0	74.7	91.1	82.9	36.3	88.0	62.2
LLaVA	50.0	65.1	57.6	78.2	63.2	70.7	7.7	63.2	35.5
LLaVA-Med (finetuned for 3 epochs)	55.5	66.5	61.0	80.5	64.2	72.4	35.9	89.2	62.5
<b>LLaVA-Tri (finetuned for 3 epochs)</b>	<b>77.1</b>	<b>86.0</b>	<b>81.6</b>	<b>86.2</b>	<b>89.3</b>	<b>87.8</b>	<b>66.5</b>	<b>99.0</b>	<b>82.8</b>

Table 4: **Comparison of different models with or without alignment pretraining with MedTrinity-25M.** The notation w/ and w/o indicate models with and without pretraining on MedTrinity-25M, respectively.

Model	Dataset Use	VQA-RAD			SLAKE			PathVQA		
		open	close	average	open	close	average	open	close	average
LLaVA-Tri	w/o	64.6	77.0	70.8	79.3	84.0	81.7	55.0	94.0	74.5
	w/	<b>77.1</b> <small>+(12.5)</small>	<b>86.0</b> <small>+(9.0)</small>	<b>81.6</b> <small>+(10.8)</small>	<b>86.2</b> <small>+(6.9)</small>	<b>89.3</b> <small>+(5.3)</small>	<b>87.8</b> <small>+(6.1)</small>	<b>66.5</b> <small>+(11.5)</small>	<b>99.0</b> <small>+(5.0)</small>	<b>82.8</b> <small>+(8.3)</small>
MiniCPM-V-2.6-8B (Yao et al., 2024)	w/o	48.5	86.4	67.5	57.2	80.0	68.6	31.2	90.5	60.9
	w/	<b>50.5</b> <small>+(2.0)</small>	<b>87.6</b> <small>+(1.2)</small>	<b>69.1</b> <small>+(1.6)</small>	<b>65.3</b> <small>+(8.1)</small>	<b>80.6</b> <small>+(0.6)</small>	<b>73.0</b> <small>+(4.4)</small>	<b>34.2</b> <small>+(3.0)</small>	<b>94.8</b> <small>+(4.3)</small>	<b>64.5</b> <small>+(3.6)</small>
InternVL2-8B (Chen et al., 2024)	w/o	38.2	76.2	57.2	61.7	77.8	69.8	16.8	86.4	51.6
	w/	<b>40.7</b> <small>+(2.5)</small>	<b>80.0</b> <small>+(3.8)</small>	<b>60.4</b> <small>+(3.2)</small>	<b>66.4</b> <small>+(4.7)</small>	<b>78.8</b> <small>+(1.0)</small>	<b>72.6</b> <small>+(2.8)</small>	<b>23.6</b> <small>+(6.8)</small>	<b>87.4</b> <small>+(1.0)</small>	<b>55.5</b> <small>+(3.9)</small>
PubMedCLIP (Eslami et al., 2023)	w/o	55.6	79.3	67.5	-	-	-	-	-	-
	w/	<b>60.6</b> <small>+(5.0)</small>	<b>79.7</b> <small>+(0.4)</small>	<b>70.2</b> <small>+(2.7)</small>	-	-	-	-	-	-

LLaVA-Tri, InternVL2-8B (Chen et al., 2024), MiniCPM-V-2.6-8B (Yao et al., 2024), and PubMedCLIP (Eslami et al., 2023). As shown in Table 4, incorporating multigranular alignment significantly enhances performance across all tested multimodal models. Notably, LLaVA-Tri exhibited improvements of 10.8%, 6.1%, and 8.3% on VQA-RAD, SLAKE, and PathVQA, respectively, compared to its counterpart without alignment. These findings underscore the potential of LLaVA-Tri as a foundational dataset capable of enhancing the medical performance of various multimodal models.

## 5 CONCLUSION

This paper introduces MedTrinity-25M, a large-scale multimodal medical dataset comprising over 25 million image-ROI-description triplets sourced from more than 30 online resources, spanning 10 modalities and covering over 65 diseases. We have developed the first automated pipeline to scale up multimodal data by generating multigranular visual and textual annotations from unpaired images. We believe that MedTrinity-25M’s enriched annotations have the potential to support a wide range of multimodal tasks, such as captioning, report generation, classification, and segmentation, as well as facilitate the large-scale pre-training of multimodal medical AI models.

## REFERENCES

- 470  
471  
472 Josh Achiam, Steven Adler, Sandhini Agarwal, Lama Ahmad, Ilge Akkaya, Florencia Leoni Aleman, Diogo  
473 Almeida, Janko Altenschmidt, Sam Altman, Shyamal Anadkat, et al. Gpt-4 technical report. *arXiv*  
474 *preprint arXiv:2303.08774*, 2023.
- 475  
476 Amir Akbarnejad, Nilanjan Ray, Penny J Barnes, and Gilbert Bigras. Predicting ki67, er, pr, and her2  
477 statuses from h&e-stained breast cancer images. *arXiv preprint arXiv:2308.01982*, 2023.
- 478  
479 Anas Awadalla, Irena Gao, Josh Gardner, Jack Hessel, Yusuf Hanafy, Wanrong Zhu, Kalyani Marathe,  
480 Yonatan Bitton, Samir Gadre, Shiori Sagawa, et al. Openflamingo: An open-source framework for training  
481 large autoregressive vision-language models. *arXiv preprint arXiv:2308.01390*, 2023.
- 482  
483 Aurelia Bustos, Antonio Pertusa, Jose-Maria Salinas, and Maria De La Iglesia-Vaya. Padchest: A large chest  
484 x-ray image dataset with multi-label annotated reports. *Medical image analysis*, 66:101797, 2020.
- 485  
486 Mathilde Caron, Hugo Touvron, Ishan Misra, Hervé Jégou, Julien Mairal, Piotr Bojanowski, and Armand  
487 Joulin. Emerging properties in self-supervised vision transformers. In *Proceedings of the IEEE/CVF*  
488 *international conference on computer vision*, pp. 9650–9660, 2021.
- 489  
490 Zhe Chen, Weiyun Wang, Hao Tian, Shenglong Ye, Zhangwei Gao, Erfei Cui, Wenwen Tong, Kongzhi Hu,  
491 Jiapeng Luo, Zheng Ma, et al. How far are we to gpt-4v? closing the gap to commercial multimodal  
492 models with open-source suites. *arXiv preprint arXiv:2404.16821*, 2024.
- 493  
494 Angel Cruz-Roa, Ajay Basavanahally, Fabio González, Hannah Gilmore, Michael Feldman, Shridar Gane-  
495 san, Natalie Shih, John Tomaszewski, and Anant Madabhushi. Automatic detection of invasive ductal  
496 carcinoma in whole slide images with convolutional neural networks. In *Medical Imaging 2014: Digital*  
497 *Pathology*. SPIE, March 2014.
- 498  
499 Maria Correia de Verdier, Rachit Saluja, Louis Gagnon, Dominic LaBella, Ujjwall Baid, Nourel Hoda Tahon,  
500 Martha Foltyn-Dumitru, Jikai Zhang, Maram Alafif, Saif Baig, et al. The 2024 brain tumor segmentation  
501 (brats) challenge: Glioma segmentation on post-treatment mri. *arXiv preprint arXiv:2405.18368*, 2024a.
- 502  
503 Maria Correia de Verdier, Rachit Saluja, Louis Gagnon, Dominic LaBella, Ujjwall Baid, Nourel Hoda Tahon,  
504 Martha Foltyn-Dumitru, Jikai Zhang, Maram Alafif, Saif Baig, et al. The 2024 brain tumor segmentation  
505 (brats) challenge: Glioma segmentation on post-treatment mri. *arXiv preprint arXiv:2405.18368*, 2024b.
- 506  
507 Kexin Ding, Mu Zhou, He Wang, Olivier Gevaert, Dimitris Metaxas, and Shaoting Zhang. A large-scale  
508 synthetic pathological dataset for deep learning-enabled segmentation of breast cancer. *Scientific Data*,  
509 10(1):231, 2023.
- 510  
511 Sedigheh Eslami, Christoph Meinel, and Gerard De Melo. Pubmedclip: How much does clip benefit visual  
512 question answering in the medical domain? In *Findings of the Association for Computational Linguistics:*  
513 *EACL 2023*, pp. 1181–1193, 2023.
- 514  
515 N. Gaggion, C. Mosquera, M. Aineseder, L. Mansilla, D. Milone, and E. Ferrante. CheXmask Database:  
516 a large-scale dataset of anatomical segmentation masks for chest x-ray images (version 0.1). <https://doi.org/10.13026/dx54-8351>, 2023.
- Nicolas Gaggion, Lucas Mansilla, Candelaria Mosquera, Diego H. Milone, and Enzo Ferrante. Improving  
anatomical plausibility in medical image segmentation via hybrid graph neural networks: applications to  
chest x-ray analysis. *IEEE Transactions on Medical Imaging*, 2022.

- 517 Jevgenij Gamper, Navid Alemi Koohbanani, Simon Graham, Mostafa Jahanifar, Ksenija Benet, Syed Ali  
518 Khurram, Ayesha Azam, Katherine Hewitt, and Nasir Rajpoot. Pannuke dataset extension, insights and  
519 baselines. *arXiv preprint arXiv:2003.10778*, 2020.
- 520  
521 Lidia Garrucho, Claire-Anne Reidel, Kaisar Kushibar, Smriti Joshi, Richard Osuala, Apostolia Tsirikoglou,  
522 Maciej Bobowicz, Javier del Riego, Alessandro Catanese, Katarzyna Gwoździewicz, et al. Mama-mia:  
523 A large-scale multi-center breast cancer dce-mri benchmark dataset with expert segmentations. *arXiv*  
524 *preprint arXiv:2406.13844*, 2024.
- 525 Ibrahim Ethem Hamamci, Sezgin Er, Furkan Almas, Ayse Gulnihani Simsek, Sevval Nil Esirgun, Irem Do-  
526 gan, Muhammed Furkan Dasdelen, Bastian Wittmann, Enis Simsar, Mehmet Simsar, et al. A foundation  
527 model utilizing chest ct volumes and radiology reports for supervised-level zero-shot detection of abnor-  
528 malities. *arXiv preprint arXiv:2403.17834*, 2024.
- 529 Xuehai He, Yichen Zhang, Luntian Mou, Eric Xing, and Pengtao Xie. Pathvqa: 30000+ questions for  
530 medical visual question answering. *arXiv preprint arXiv:2003.10286*, 2020a.
- 531  
532 Y He, G Yang, J Yang, Y Chen, Y Kong, J Wu, L Tang, X Zhu, JL Dillenseger, P Shao, S Zhang, H Shu,  
533 JL Coatrieux, and S Li. Dense biased networks with deep priori anatomy and hard region adaptation:  
534 Semisupervised learning for fine renal artery segmentation. *Medical Image Analysis*, 63, 2020b.
- 535 Yuting He, Guanyu Yang, Jian Yang, Rongjun Ge, Youyong Kong, Xiaomei Zhu, Shaobo Zhang, Pengfei  
536 Shao, Huazhong Shu, Jean-Louis Dillenseger, Jean-Louis Coatrieux, and Shuo Li. Meta grayscale adap-  
537 tive network for 3D integrated renal structures segmentation. *Med. Image Anal.*, 71:102055, July 2021.
- 538  
539 Wisdom Ikezogwo, Saygin Seyfioglu, Fatemeh Ghezloo, Dylan Geva, Fatwir Sheikh Mohammed, Pavan Ku-  
540 mar Anand, Ranjay Krishna, and Linda Shapiro. Quilt-1m: One million image-text pairs for histopathol-  
541 ogy. *Advances in Neural Information Processing Systems*, 36, 2024.
- 542 Jeremy Irvin, Pranav Rajpurkar, Michael Ko, Yifan Yu, Silvana Ciurea-Ilcus, Chris Chute, Henrik Mark-  
543 lund, Behzad Haghgo, Robyn Ball, Katie Shpanskaya, et al. Chexpert: A large chest radiograph dataset  
544 with uncertainty labels and expert comparison. In *Proceedings of the AAAI conference on artificial intel-*  
545 *ligence*, volume 33, pp. 590–597, 2019.
- 546 Andrew Janowczyk and Anant Madabhushi. Deep learning for digital pathology image analysis: A compre-  
547 hensive tutorial with selected use cases. *Journal of pathology informatics*, 7(1):29, 2016.
- 548  
549 Di Jin, Eileen Pan, Nassim Oufattole, Wei-Hung Weng, Hanyi Fang, and Peter Szolovits. What disease does  
550 this patient have? a large-scale open domain question answering dataset from medical exams. *Applied*  
551 *Sciences*, 11(14):6421, 2021.
- 552 Qiao Jin, Won Kim, Qingyu Chen, Donald C Comeau, Lana Yeganova, W John Wilbur, and Zhiyong Lu.  
553 Medcpt: Contrastive pre-trained transformers with large-scale pubmed search logs for zero-shot biomed-  
554 ical information retrieval. *Bioinformatics*, 39(11):btad651, 2023.
- 555 Alistair EW Johnson, Tom J Pollard, Nathaniel R Greenbaum, Matthew P Lungren, Chih-ying Deng, Yifan  
556 Peng, Zhiyong Lu, Roger G Mark, Seth J Berkowitz, and Steven Horng. MIMIC-CXR-JPG, a large publicly  
557 available database of labeled chest radiographs. *arXiv preprint arXiv:1901.07042*, 2019a.
- 558  
559 AlistairEW Johnson, TomJ Pollard, SethJ Berkowitz, NathanielR Greenbaum, MatthewP Lungren, Chih-  
560 ying Deng, RogerG Mark, and Steven Horng. MIMIC-CXR, a de-identified publicly available database of  
561 chest radiographs with free-text reports. *Scientific data*, 6(1):317, 2019b.
- 562 Jeff Johnson, Matthijs Douze, and Hervé Jégou. Billion-scale similarity search with gpus. *IEEE Transactions*  
563 *on Big Data*, 7(3):535–547, 2019c.

- 564 Jared Kaplan, Sam McCandlish, Tom Henighan, Tom B Brown, Benjamin Chess, Rewon Child, Scott Gray,  
565 Alec Radford, Jeffrey Wu, and Dario Amodei. Scaling laws for neural language models. *arXiv preprint*  
566 *arXiv:2001.08361*, 2020.
- 567 Alexandros Karargyris, Renato Umeton, Micah J Sheller, Alejandro Aristizabal, Johnu George, Anna Wuest,  
568 Sarthak Pati, Hasan Kassem, Maximilian Zenk, Ujjwal Baid, et al. Federated benchmarking of medical  
569 artificial intelligence with medperf. *Nature Machine Intelligence*, 5(7):799–810, 2023.
- 570 Jakob Nikolas Kather, Niels Halama, and Alexander Marx. 100,000 histological images of human colorectal  
571 cancer and healthy tissue. <https://doi.org/10.5281/zenodo.1214456>, 2018.
- 572 Masakata Kawai, Noriaki Ota, and Shinsuke Yamaoka. Large-scale pretraining on pathological images for  
573 fine-tuning of small pathological benchmarks. In *Workshop on Medical Image Learning with Limited and*  
574 *Noisy Data*, pp. 257–267. Springer, 2023.
- 575 Jason J Lau, Soumya Gayen, Asma Ben Abacha, and Dina Demner-Fushman. A dataset of clinically gener-  
576 ated visual questions and answers about radiology images. *Scientific data*, 5(1):1–10, 2018a.
- 577 Jason J Lau, Soumya Gayen, Asma Ben Abacha, and Dina Demner-Fushman. A dataset of clinically gener-  
578 ated visual questions and answers about radiology images. *Scientific data*, 5(1):1–10, 2018b.
- 579 Chunyuan Li, Cliff Wong, Sheng Zhang, Naoto Usuyama, Haotian Liu, Jianwei Yang, Tristan Nau-  
580 mann, Hoifung Poon, and Jianfeng Gao. Llava-med: Training a large language-and-vision assistant for  
581 biomedicine in one day. *Advances in Neural Information Processing Systems*, 36, 2024a.
- 582 Chunyuan Li, Cliff Wong, Sheng Zhang, Naoto Usuyama, Haotian Liu, Jianwei Yang, Tristan Nau-  
583 mann, Hoifung Poon, and Jianfeng Gao. Llava-med: Training a large language-and-vision assistant for  
584 biomedicine in one day. *Advances in Neural Information Processing Systems*, 36, 2024b.
- 585 Weixiong Lin. axiong/pmc\_oa datasets at hugging face. [https://huggingface.co/datasets/](https://huggingface.co/datasets/axiong/pmc_oa)  
586 *axiong/pmc\_oa*, 2023.
- 587 Weixiong Lin, Ziheng Zhao, Xiaoman Zhang, Chaoyi Wu, Ya Zhang, Yanfeng Wang, and Weidi Xie. Pmc-  
588 clip: Contrastive language-image pre-training using biomedical documents. In *International Conference*  
589 *on Medical Image Computing and Computer-Assisted Intervention*, pp. 525–536. Springer, 2023.
- 590 Bo Liu, Li-Ming Zhan, Li Xu, Lin Ma, Yan Yang, and Xiao-Ming Wu. Slake: A semantically-labeled  
591 knowledge-enhanced dataset for medical visual question answering. In *2021 IEEE 18th International*  
592 *Symposium on Biomedical Imaging (ISBI)*, pp. 1650–1654. IEEE, 2021.
- 593 Haotian Liu, Chunyuan Li, Qingyang Wu, and Yong Jae Lee. Visual instruction tuning. *Advances in neural*  
594 *information processing systems*, 36, 2024.
- 595 Meng Lou, Hanning Ying, Xiaoqing Liu, Hong-Yu Zhou, Yuqing Zhang, and Yizhou Yu. Sdr-former: A  
596 siamese dual-resolution transformer for liver lesion classification using 3d multi-phase imaging. *arXiv*  
597 *preprint arXiv:2402.17246*, 2024.
- 598 Jun Ma and Bo Wang. Miccai flare23: Fast, low-resource, and accurate organ and pan-cancer segmenta-  
599 tion in abdomen ct, Apr 2023. URL [https://codalab.lisn.upsaclay.fr/competitions/](https://codalab.lisn.upsaclay.fr/competitions/12239)  
600 *12239*.
- 601 Michael Moor, Qian Huang, Shirley Wu, Michihiro Yasunaga, Yash Dalmia, Jure Leskovec, Cyril Zakka,  
602 Eduardo Pontes Reis, and Pranav Rajpurkar. Med-flamingo: a multimodal medical few-shot learner. In  
603 *Machine Learning for Health (ML4H)*, pp. 353–367. PMLR, 2023.

- 611 Obioma Pelka, Sven Koitka, Johannes Rückert, Felix Nensa, and Christoph M Friedrich. Radiology objects  
612 in context (roco): a multimodal image dataset. In *Intravascular Imaging and Computer Assisted Stenting*  
613 *and Large-Scale Annotation of Biomedical Data and Expert Label Synthesis: 7th Joint International*  
614 *Workshop, CVII-STENT 2018 and Third International Workshop, LABELS 2018, Held in Conjunction*  
615 *with MICCAI 2018, Granada, Spain, September 16, 2018, Proceedings 3*, pp. 180–189. Springer, 2018.  
616
- 617 Eduardo Pontes Reis, Felipe Nascimento, Mateus Aranha, Fernando Mainetti Secol, Birajara Machado,  
618 Marcelo Felix, Anouk Stein, and Edson Amaro. Brain hemorrhage extended (bhx): Bounding box extrap-  
619 olation from thick to thin slice ct images. *PhysioNet*, 101(23):e215–20, 2020.
- 620 Khaled Saab, Tao Tu, Wei-Hung Weng, Ryutaro Tanno, David Stutz, Ellery Wulczyn, Fan Zhang, Tim  
621 Strother, Chunjong Park, Elahe Vedadi, et al. Capabilities of gemini models in medicine. *arXiv preprint*  
622 *arXiv:2404.18416*, 2024.  
623
- 624 Pengfei Shao, Chao Qin, Changjun Yin, Xiaoxin Meng, Xiaobing Ju, Jie Li, Qiang Lv, Wei Zhang, and  
625 Zhengquan Xu. Laparoscopic partial nephrectomy with segmental renal artery clamping: technique and  
626 clinical outcomes. *Eur. Urol.*, 59(5):849–855, May 2011.
- 627 Pengfei Shao, Lijun Tang, Pu Li, Yi Xu, Chao Qin, Qiang Cao, Xiaobing Ju, Xiaoxin Meng, Qiang Lv,  
628 Jie Li, Wei Zhang, and Changjun Yin. Precise segmental renal artery clamping under the guidance of  
629 dual-source computed tomography angiography during laparoscopic partial nephrectomy. *Eur. Urol.*, 62  
630 (6):1001–1008, December 2012.  
631
- 632 Baifeng Shi, Ziyang Wu, Maolin Mao, Xin Wang, and Trevor Darrell. When do we not need larger vision  
633 models? *arXiv preprint arXiv:2403.13043*, 2024.  
634
- 635 Carsen Stringer and Marius Pachitariu. Cellpose3: one-click image restoration for improved cellular seg-  
636 mentation. *bioRxiv*, pp. 2024–02, 2024.
- 637 Gemini Team, Rohan Anil, Sebastian Borgeaud, Yonghui Wu, Jean-Baptiste Alayrac, Jiahui Yu, Radu Sori-  
638 cut, Johan Schalkwyk, Andrew M Dai, Anja Hauth, et al. Gemini: a family of highly capable multimodal  
639 models. *arXiv preprint arXiv:2312.11805*, 2023a.  
640
- 641 Gemini Team, Rohan Anil, Sebastian Borgeaud, Yonghui Wu, Jean-Baptiste Alayrac, Jiahui Yu, Radu Sori-  
642 cut, Johan Schalkwyk, Andrew M Dai, Anja Hauth, et al. Gemini: a family of highly capable multimodal  
643 models. *arXiv preprint arXiv:2312.11805*, 2023b.
- 644 Meta LLaMA Team. Introducing meta llama 3: The most capable openly available llm to date. <https://ai.meta.com/blog/meta-llama-3/>, 2024.  
645  
646
- 647 Yuri Tolkach, Lisa Marie Wolgast, Alexander Damanakis, Alexey Pryalukhin, Simon Schallenberg, Wolf-  
648 gang Hulla, Marie-Lisa Eich, Wolfgang Schroeder, Anirban Mukhopadhyay, Moritz Fuchs, et al. Artificial  
649 intelligence for tumour tissue detection and histological regression grading in oesophageal adenocarci-  
650 nomas: a retrospective algorithm development and validation study. *The Lancet Digital Health*, 5(5):  
651 e265–e275, 2023.
- 652 Masayuki Tsuneki and Fahdi Kanavati. Inference of captions from histopathological patches. In *Internat-*  
653 *ional Conference on Medical Imaging with Deep Learning*, pp. 1235–1250. PMLR, 2022.  
654
- 655 Tao Tu, Shekoofeh Azizi, Danny Driess, Mike Schaekermann, Mohamed Amin, Pi-Chuan Chang, Andrew  
656 Carroll, Charles Lau, Ryutaro Tanno, Ira Ktena, et al. Towards generalist biomedical ai. *NEJM AI*, 1(3):  
657 AIOa2300138, 2024a.

- 658 Tao Tu, Shekoofeh Azizi, Danny Driess, Mike Schaekermann, Mohamed Amin, Pi-Chuan Chang, Andrew  
659 Carroll, Charles Lau, Ryutarō Tanno, Ira Ktena, et al. Towards generalist biomedical ai. *NEJM AI*, 1(3):  
660 AIoa2300138, 2024b.
- 661 Patrick Wagner, Maximilian Springenberg, Marius Kröger, Rose KC Moritz, Johannes Schleusener, Mar-  
662 tina C Meinke, and Jackie Ma. Semantic modeling of cell damage prediction: a machine learning ap-  
663 proach at human-level performance in dermatology. *Scientific Reports*, 13(1):8336, 2023.
- 664 Jiacheng Wang, Lan Wei, Liansheng Wang, Qichao Zhou, Lei Zhu, and Jing Qin. Boundary-aware trans-  
665 formers for skin lesion segmentation. In *Medical Image Computing and Computer Assisted Intervention–*  
666 *MICCAI 2021: 24th International Conference, Strasbourg, France, September 27–October 1, 2021, Pro-*  
667 *ceedings, Part I 24*, pp. 206–216. Springer, 2021.
- 669 Xiaosong Wang, Yifan Peng, Le Lu, Zhiyong Lu, Mohammadhadi Bagheri, and Ronald M Summers.  
670 ChestX-Ray8: Hospital-scale chest x-ray database and benchmarks on weakly-supervised classification  
671 and localization of common thorax diseases. In *2017 IEEE Conference on Computer Vision and Pattern*  
672 *Recognition (CVPR)*. IEEE, July 2017a.
- 673 Xiaosong Wang, Yifan Peng, Le Lu, Zhiyong Lu, Mohammadhadi Bagheri, and Ronald M Summers.  
674 ChestX-Ray8: Hospital-scale chest x-ray database and benchmarks on weakly-supervised classification  
675 and localization of common thorax diseases. In *2017 IEEE Conference on Computer Vision and Pattern*  
676 *Recognition (CVPR)*. IEEE, July 2017b.
- 677 Xiaosong Wang, Yifan Peng, Le Lu, Zhiyong Lu, Mohammadhadi Bagheri, and Ronald M Summers.  
678 ChestX-ray: Hospital-scale chest x-ray database and benchmarks on weakly supervised classification and  
679 localization of common thorax diseases. In *Deep Learning and Convolutional Neural Networks for Medi-*  
680 *cal Imaging and Clinical Informatics*, Advances in computer vision and pattern recognition, pp. 369–392.  
681 Springer International Publishing, Cham, 2019.
- 682 Guangzhi Xiong, Qiao Jin, Zhiyong Lu, and Aidong Zhang. Benchmarking retrieval-augmented generation  
683 for medicine. *arXiv preprint arXiv:2402.13178*, 2024.
- 684 Ke Yan, Xiaosong Wang, Le Lu, and Ronald M Summers. Deeplesion: Automated deep mining, catego-  
685 rization and detection of significant radiology image findings using large-scale clinical lesion annotations.  
686 *arXiv preprint arXiv:1710.01766*, 2017a.
- 687 Ke Yan, Xiaosong Wang, Le Lu, and Ronald M Summers. Deeplesion: Automated deep mining, catego-  
688 rization and detection of significant radiology image findings using large-scale clinical lesion annotations.  
689 *arXiv preprint arXiv:1710.01766*, 2017b.
- 690 Jiancheng Yang, Rui Shi, Donglai Wei, Zequan Liu, Lin Zhao, Bilian Ke, Hanspeter Pfister, and Bingbing  
691 Ni. Medmnist v2-a large-scale lightweight benchmark for 2d and 3d biomedical image classification.  
692 *Scientific Data*, 10(1):41, 2023.
- 693 Yuan Yao, Tianyu Yu, Ao Zhang, Chongyi Wang, Junbo Cui, Hongji Zhu, Tianchi Cai, Haoyu Li, Weilin  
694 Zhao, Zhihui He, et al. Minicpm-v: A gpt-4v level mllm on your phone. *arXiv preprint arXiv:2408.01800*,  
695 2024.
- 696 Jin Ye, Junlong Cheng, Jianpin Chen, Zhongying Deng, Tianbin Li, Haoyu Wang, Yanzhou Su, Ziyang Huang,  
697 Jilong Chen, Lei Jiang, et al. Sa-med2d-20m dataset: Segment anything in 2d medical imaging with 20  
698 million masks. *arXiv preprint arXiv:2311.11969*, 2023.
- 699 Sheng Zhang, Yanbo Xu, Naoto Usuyama, Hanwen Xu, Jaspreet Bagga, Robert Tinn, Sam Preston, Rajesh  
700 Rao, Mu Wei, Naveen Valluri, et al. Biomedclip: a multimodal biomedical foundation model pretrained  
701 from fifteen million scientific image-text pairs. *arXiv preprint arXiv:2303.00915*, 2023a.

705 Xiaoman Zhang, Chaoyi Wu, Ziheng Zhao, Weixiong Lin, Ya Zhang, Yanfeng Wang, and Weidi Xie. Pmc-  
706 vqa: Visual instruction tuning for medical visual question answering. *arXiv preprint arXiv:2305.10415*,  
707 2023b.

708  
709 Xiaoman Zhang, Chaoyi Wu, Ziheng Zhao, Jiayu Lei, Ya Zhang, Yanfeng Wang, and Weidi Xie.  
710 Radgenome-chest ct: A grounded vision-language dataset for chest ct analysis. *arXiv preprint*  
711 *arXiv:2404.16754*, 2024.

712 Ziheng Zhao, Yao Zhang, Chaoyi Wu, Xiaoman Zhang, Ya Zhang, Yanfeng Wang, and Weidi Xie. One  
713 model to rule them all: Towards universal segmentation for medical images with text prompts. *arXiv*  
714 *preprint arXiv:2312.17183*, 2023.

715  
716 Hong-Yu Zhou, Subathra Adithan, Julián Nicolás Acosta, Eric J Topol, and Pranav Rajpurkar. A generalist  
717 learner for multifaceted medical image interpretation. *arXiv preprint arXiv:2405.07988*, 2024.

718  
719  
720  
721  
722  
723  
724  
725  
726  
727  
728  
729  
730  
731  
732  
733  
734  
735  
736  
737  
738  
739  
740  
741  
742  
743  
744  
745  
746  
747  
748  
749  
750  
751



## APPENDIX

We present the following items in the Appendix:

1. Data source about MedTrinity-25M. (Section A)
2. Quantitative comparison between GPT-4V and LLaVA-Medcap (Section B).
3. Examples of ROI for normal regions and multiple regions.(Section C).
4. The list of expert ROI models (Section D).
5. Details of LLM Evaluation of Alignment (Section E).
6. Prompt for generating MedTrinity-25M. (Section F).

## A DATA SOURCE

Table 5: Data sources for MedTrinity-25M from various medical image datasets, detailing their modalities, biological structures, quantities, and annotations.

Dataset Name	Modality	Biological Structures	Quantity	Text	Disease Type	BBox	Mask
BHX(Reis et al., 2020)	MRI	brain	973908	✗	✗	✗	✓
BRATS24-MICCAI(de Verdier et al., 2024b)	MRI	brain	2535132	✗	✗	✓	✗
BRATS-ISBI(Karargyris et al., 2023)	MRI	brain	987340	✗	✗	✓	✗
breast histopathology(Janowczyk & Madab-hushi, 2016; Cruz-Roa et al., 2014)	Histopathology	breast	547403	✗	✓	✗	✗
BreastCancer(Ding et al., 2023)	Histopathology	breast	1824	✗	✗	✓	✗
CheXpert(Irvin et al., 2019)	X-Ray	lung	183242	✗	✓	✗	✗
CISC(Gamper et al., 2020)	Histopathology	Adrenal, Bile duct, Bladder, Breast, Colon, Cervix, Esophagus Kidney, Liver,etc	16285	✗	✓	✓	✗
CPD(Wagner et al., 2023)	Histopathology	skin	204	✗	✗	✓	✗
CT-RATE(Hamamci et al., 2024)	CT	lung, liver, mediastinum, kidney, heart, etc.	3869640	✓	✗	✗	✗
DeepLesion(Yan et al., 2017b)	CT	bone, abdomen, mediastinum, liver, lung, kidney, soft tissue, pelvis	2889672	✗	✗	✗	✓

Table 5 : Continued from previous page

Dataset Name	Modality	Biological Structures	Quantity	Text	Disease Type	BBox	Mask
FLARE23(Ma & Wang, 2023)	CT	Liver, kidney, spleen, pancreas, Aorta, adrenal gland, Gallbladder, esophagus, stomach, duodenum,etc.	13770	✗	✓	✓	✗
ihc4bc(Akbarnejad et al., 2023)	Microscopy	cell	102535	✗	✓	✗	✗
KIPA22(Shao et al., 2012; 2011; He et al., 2020b; 2021)	CT	kidney, cervix	26878	✗	✗	✓	✗
LLaVA-Med(Li et al., 2024b)	CT, MR, Endoscopy, X-Ray, Ultrasound, Histopathology, Dermoscopy, Microscopy, Fundus, PET	cell, rib, tissue, face, brain, vascular, liver, bone, lymph, etc.	22550	✓	✗	✗	✗
LLD-MMRI(Lou et al., 2024)	MRI	liver	21523	✗	✗	✓	✗
MAMA-MIA(Garrucho et al., 2024)	MRI	breast	316113	✗	✗	✓	✗
MIMIC-CXR-JPG(Johnson et al., 2019a)	X-Ray	lung	240506	✓	✓	✗	✓
NCT-CRC-HE-100K(Kather et al., 2018)	Histopathology	colon	100361	✗	✓	✗	✗
NIH-CXR(Wang et al., 2017a;b; 2019)	X-Ray	lung	986	✗	✗	✗	✓
PadChest(Bustos et al., 2020)	CT	lung	96284	✓	✗	✗	✗
PatchGastricADC22(Tsuneki & Kanavati, 2022)	MRI	brain	98399	✗	✓	✗	✗
Path-VQA training(He et al., 2020a)	Pathology	gastrointestinal, colon, appendix, pinworm,etc.	13375	✓	✓	✗	✗
PMC-OA(Lin, 2023)	CT, MR, Endoscopy, X-Ray, Ultrasound, Histopathology, Dermoscopy, Microscopy, Fundus, PET	cell, tissue, vascular, brain, bone, liver, lymph, eye, epithelium, etc.	856999	✓	✗	✗	✗

Table 5 : Continued from previous page

Dataset Name	Modality	Biological Structures	Quantity	Text	Disease Type	BBox	Mask
PMC-VQA(Zhang et al., 2023b)	CT, MR, Endoscopy, X-Ray, Ultrasound, Histopathology, Dermoscopy, Microscopy, Fundus, PET	cell, brain, tissue, artery, bone, face, rib, vascular, liver, eye, etc.	144999	✓	✗	✗	✗
PTCGA(Kawai et al., 2023)	Histopathology	brain, breast, uterine corpus, kidney, lung, thyroid	3293965	✗	✓	✓	✗
Quilt-1M(Ikezogwo et al., 2024)	Histopathology	skin, lung, soft tissue, blood, kidney, bone, etc.	643819	✓	✗	✗	✗
SAMMed-20M(Ye et al., 2023)	X-Ray, PET, CT, MR, Endoscopy, dermoscopy	brain, kidney, liver, lung, pancreas, pulmonary, hepatic, skin, etc.	5491274	✗	✓	✓	✗
SLAKE training(Liu et al., 2021)	CT, MRI, X-Ray	brain, liver, kidney, pelvic, lung	646	✓	✓	✓	✗
TCGA(Kawai et al., 2023)	Histopathology	tissue	1142221	✗	✗	✓	✗
ULS23	CT	lung, lymph nodes, bladder, brain, colon, kidney, lung.	105669	✗	✗	✓	✗
VALSET(Tolkach et al., 2023)	Histopathology	oesophagus, stomach	277565	✗	✓	✗	✗
VQA-RAD training(Lau et al., 2018b)	X-Ray, MRI	brain, lung, abdomen,etc.	1758	✓	✓	✗	✗
<b>Total</b>			<b>25016845</b>				

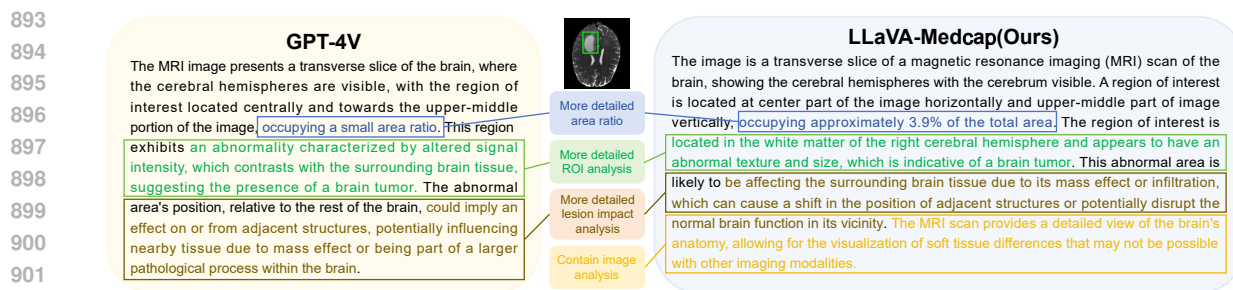
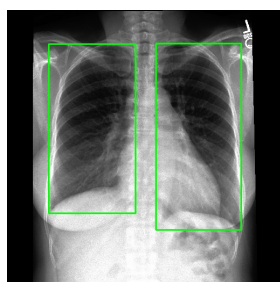
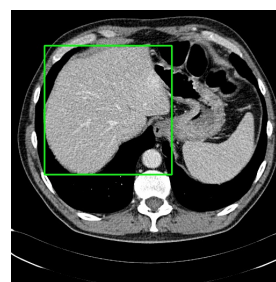


Figure 9: **Qualitative Comparison with sample generated by GPT-4V.** Compared to GPT-4V, our model generate more detailed caption.



(a) A no infection sample from MIMIC-CXR. The ROIs highlight the left and right lungs.



(b) A healthy sample from SLAKE. The ROI points out the liver.

Figure 10: Examples of ROIs for normal regions.

## B QUANTITATIVE COMPARISON OF LLaVA-MEDCAP WITH GPT-4V

As detailed in Section 3.2.2 of the main paper, we developed an enhanced version of LLaVA (Li et al., 2024a), called LLaVA-Medcap. This enhancement leverages the latest LLaMA3 (Team, 2024) to boost linguistic capabilities and incorporates multi-scale feature extraction (Shi et al., 2024) to improve vision capabilities.

To justify the selection of our specialized medical model, LLaVA-Tri, over GPT-4V for generating textual descriptions, we conducted a quantitative comparison of the outputs generated by both models. We assessed the level of detail by comparing the average word count of text descriptions generated for the same sample. LLaVA-Tri, after task-specific fine-tuning, outperformed GPT-4V by 3.6% in word count, indicating that the descriptions generated by LLaVA-Medcap are more detailed. We also provide a qualitative comparison with sample generated by LLaVA-Tri and GPT-4V in Figure 9. Based on these findings, we selected LLaVA-Medcap to generate multigranular textual descriptions for our entire MedTrinity-25M.

## C EXAMPLES OF ROIS

As described in Section 3.1 of the main paper, the ROIs identified by expert grounding models predominantly capture pathological features such as lesions, inflammation, neoplasms, infections, or other potential abnormalities. In rare cases where no abnormalities are found, the ROIs typically focus on the primary object or organ in the image. Examples of such normal ROIs are presented in Figure 10.

940  
941  
942  
943  
944  
945  
946  
947  
948  
949  
950  
951  
952  
953  
954  
955  
956  
957  
958  
959  
960  
961  
962  
963  
964  
965  
966  
967  
968  
969  
970  
971  
972  
973  
974  
975  
976  
977  
978  
979  
980  
981  
982  
983  
984  
985  
986

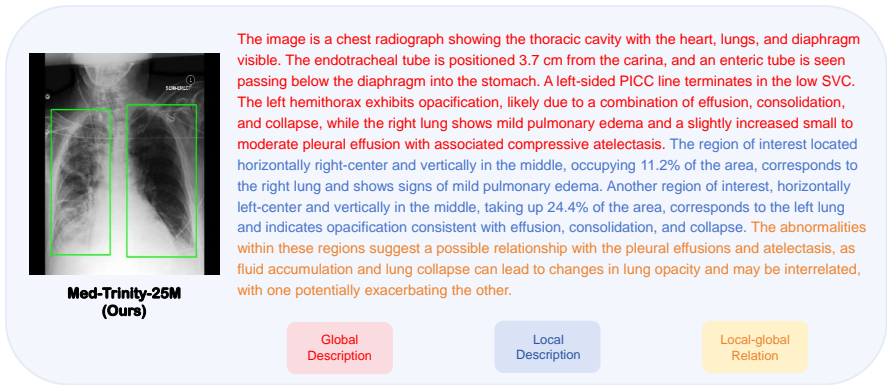


Figure 11: A chest radiography example where global information matters. The diagnosis in this case requires a comprehensive analysis of the entire image, encompassing both the left and right lungs. Here, ROIs encompass the large lesion areas of left and right lungs. Detailed local texture analysis of each region contributes to the overall global diagnosis

In some instances where global context is also critical for disease identification, the ROIs encompass multiple lesion areas, integrating both global and local information. For example, in chest radiography, analyzing both lungs and their overall structure is often essential for accurate diagnosis, as shown in Figure 11. By providing multigranular annotations that incorporate both local and global perspectives, our dataset helps multigranular alignment for medical foundation models.

## D LIST OF EXPERT MODELS TO LOCATE ROIS

As detailed in Section 3.2.1 of the main paper, for datasets lacking localization information such as segmentation masks and bounding boxes, we employ various pretrained expert models to identify the ROIs. The specific expert models used for each dataset are listed in Table 6.

## E DETAILS OF LLM EVALUATION OF ALIGNMENT

An example of perfect alignment score results evaluated by GPT-4V is shown in Figure 12. In these examples, GPT-4V fully aligned with human annotations across all five criteria, resulting in perfect alignment scores. The prompt used to query GPT-4V for evaluating the alignment score is shown in Figure 13 of supplementary.

The prompt used to query GPT-4V for evaluating the alignment score is shown in Figure 13.

## F PROMPT TEMPLATE FOR GENERATION OF MULTIGRANULAR TEXT DESCRIPTION

To generate multigranular textual descriptions, we design a multi-task prompting approach, breaking down this task into several smaller descriptive tasks. The model’s responses to these different tasks collectively form the final fine-grained text description.

Figure 14 illustrates our prompt template consisting of a three-level hierarchical framework with questions to instruct MLLMs:

Table 6: List of expert models used to generate ROIs for different datasets.

ID	Dataset Name	Model
1	breast histopathology	HoverNet (Stringer & Pachitariu, 2024)
2	BreastCancer	
3	CISC	
4	CPD	
5	NCT-CRC-HE-100K	
6	PTCGA	
7	TCGA	
8	VALSET	
9	ihc4bc	
10	Quilt-1M	
11	CT-RATE	SAT (Zhao et al., 2023)
12	PMC-OA	DINO (Caron et al., 2021)
13	PMC-VQA	
14	LLaVA-Med	
15	Path-VQA training	
16	PadChest	CheXmask (Gaggion et al., 2023) (Gaggion et al., 2022)
17	MIMIC-CXR-JPG	
18	CheXpert	

**Step 1 - Global Understanding:** Instruct MLLMs to provide a comprehensive description of the image, detailing all modalities, identified anatomical structures, and their approximate locations. This step ensures that MLLMs gains an overarching understanding and basic information about the image.

**Step 2 - Local Analysis:** Instruct MLLMs to conduct a detailed analysis of the regions of interest (ROI), including their locations, abnormalities, and textures. This step guides MLLMs to focus on specific lesions for a thorough assessment.

**Step 3 - Region-wise Correlations:** Instruct MLLMs to examine the relationship between different regions and predict how the surrounding areas will be affected by the lesions in the ROI. This step aims to understand the interaction between local and global attributes, assessing the impact of local abnormalities on the entire organ for accurate disease diagnosis.

1034  
1035  
1036  
1037  
1038  
1039  
1040  
1041  
1042  
1043  
1044  
1045  
1046  
1047  
1048  
1049  
1050  
1051  
1052  
1053  
1054  
1055  
1056  
1057  
1058  
1059  
1060  
1061  
1062  
1063  
1064  
1065  
1066  
1067  
1068  
1069  
1070  
1071  
1072  
1073  
1074  
1075  
1076  
1077  
1078  
1079  
1080

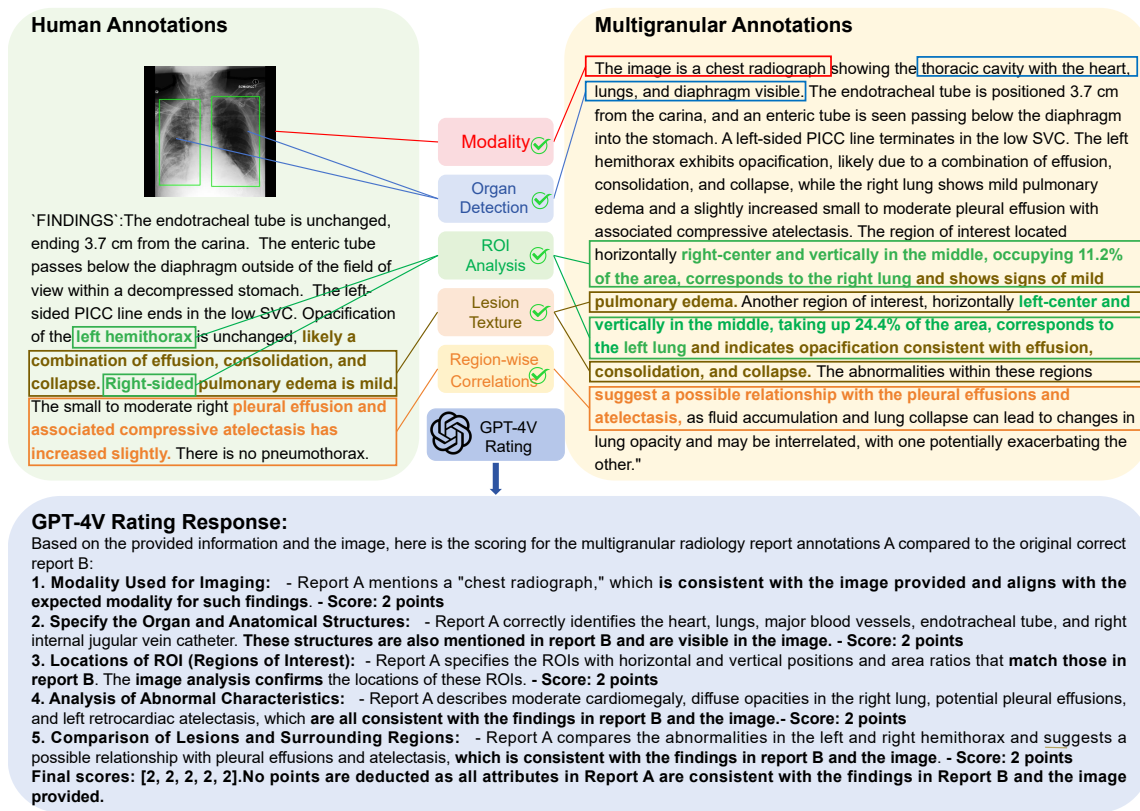


Figure 12: An example of a perfect score result evaluated by GPT-4V. GPT-4V assesses five criteria, each fully aligned with human annotations, resulting in perfect scores.

1081  
1082  
1083  
1084  
1085  
1086  
1087  
1088  
1089  
1090  
1091  
1092  
1093  
1094  
1095  
1096  
1097  
1098  
1099  
1100  
1101  
1102  
1103  
1104  
1105  
1106  
1107  
1108  
1109  
1110  
1111  
1112  
1113  
1114  
1115  
1116  
1117  
1118  
1119  
1120  
1121  
1122  
1123  
1124  
1125  
1126  
1127

**Prompting MLLMs to evaluate the alignment of generated multi-granular annotations with human annotations**

Let's think it step by step. Evaluate the multigranular radiology report annotations (Report A) compared to the radiology report B step by step. Both reports are based on the same image. Follow these guidelines to ensure accurate assessment:

**Note:** If neither the original question nor radiology report B mentions any abnormalities or diseases, such as "the lungs are clear without confluent consolidation or effusion" or "no pneumothorax is seen", skip the evaluation and return "None."

**Basic Rating Rules:**

- Evaluate each attribute in Report A against radiology report B and verify the information by analyzing the image. Do not deduct points without image analysis.
- Judge correctness based on the accuracy of medical facts and diagnoses, not on the exact alignment of sentence structure or organization.
- If radiology report B does not mention any abnormalities or diseases, skip the evaluation and return "None," such as "the lungs are clear without confluent consolidation or effusion" or "no pneumothorax is seen".
- Each of the 5 attributes should be judged independently. Errors in one attribute should not affect the scoring of other attributes.

**Attributes and Corresponding Rating Rules:**

- Modality Used for Imaging:**
  - Rating Rule:** Compare with radiology report B. Different names for the same modality (e.g., "chest X-ray" and "CXR") are acceptable.
- Specify the Organ and Anatomical Structures:**
  - Rating Rule:** Check if the organs and anatomical structures in Report A match those in radiology report B or appear in the image.
    - Mentioned in both: 2 points
    - Mentioned in one: 1 point
    - Not mentioned in either: 0 points
    - Do not deduct points without image analysis.
- Locations of ROI (Regions of Interest):**
  - Rating Rule:** Compare the "horizontal" and "vertical" positions, and the "area ratio" of ROIs with radiology report B. A 5% error in the area ratio is acceptable. If Report A includes at least one ROI from radiology report B, no points are deducted, even if all ROIs are not covered.
- Analysis of Abnormal Characteristics:**
  - Rating Rule:** Characteristics indicating pathology should match those in radiology report B or appear in the image.
    - Mentioned in both: 2 points
    - Mentioned in one: 1 point
    - Not mentioned in either: 0 points
    - Do not deduct points without image analysis.
- Comparison of Lesions and Surrounding Regions:**
  - Rating Rule:** Differences in features and disease progression should match those in radiology report B or appear in the image.
    - Mentioned in both: 2 points
    - Mentioned in one: 1 point
    - Not mentioned in either: 0 points
    - Do not deduct points without image analysis.

**Note:** Return the scores in a list. For example, if attributes 4 and 5 get deducted 1 point each, while others score 2 points each, return [2, 2, 2, 1, 1]. Provide a short reason (within 80 words) for each point deduction.

Figure 13: Prompt used to evaluate the alignment of generated multigranular textual descriptions.



**Prompting MLLMs to generate multigranular textual description**

```

caption_template = Template("<image>
`Caption of the image` : {{caption}}
`Disease or organ` : {{disease}}
`Specific position` : {{descs}}
`Knowledge` : {{knowledge}}
You are provided with a biomedical image from a medical dataset, the disease type (or organ name if there is no disease) of the dataset ('Disease or organ'), the medical Knowledge of the disease ('Knowledge') and a coarse caption ('Caption') of the image. In addition, the green bounding box and its specific position in the image ('Specific position') are given, indicating appearance of disease. If no green bounding box, there is no disease.
Your task is to answer the following questions based on the image, green bounding box, caption, disease type and disease knowledge, and condense your answers into caption-styled text.
### question1
Give me a detailed description of the image, including type of the image, organs in the image, approximate location of these organs and relevant locations of these organs and any medical devices (if present) visible in the image as detailedly as possible.
Note when answering question1:
1. Not all disease knowledge is relevant to this image; only utilize disease knowledge pertinent to the condition depicted in this image for analysis.
2. The coarse caption may not explicitly describe the image, for example, there may appear multiple organs in the caption. You should utilize your knowledge to figure out the most ONE organ and ONE disease to give your description.
3. Your answer should not contain anything about the green bounding box like the contour itself and its outline.
4. Do not explain or emphasize your analysis.
### question2
Specify the specific location of the green bounding box in the image and its relative position to other reference objects in the image. Describe what is unusual in the green bounding box indicating the disease (color, texture, size and other features) .
Note when answering question2:
1. "specific location" is the given parameter `Specific position` but "relative position" is not provided.
2. There may be multiple green bounding boxes, and the contents of these contours may not necessarily represent the affected areas. Therefore, you need to first answer the questions based on the contents within each green bounding box. Afterward, analyze the location of the disease based on your answers.
3. Do not use phrase "green bounding box" in your response, use "region of interest" as a substitution. Do not contain phrases "caption", "medical annotation", "medical knowledge".
4. Do not say anything that is not needed in your analysis, like introduction of the disease and medical equipments.
5. Do not explain or emphasize your analysis.
### question3
What may be the relationship between the content in the green bounding box and other regions (others being cause of the disease/jointly affected by the diseases/one affect the others/relative positional relationships)? Why and is it possible?
Note when answering question3:
1. Utilize external knowledge, if possible, to choose relationships and give necessary analysis.
2. You can only give an explanation to your choice within two sentences.
3. Do not summarize what you've said.
4. Do not emphasize your analysis.
### Integrate Information
Describe your answers in a descriptive sentence, not in a "Question-Answer" style. Combine and slightly shorten your answers to the above three questions into a coherent text, keeping as much information of your answers as possible.
Note when integrating information and outputting your response:
1. Don't respond saying you're unable to assist with requests.
2. You should only output your combined and shortened text.
")
prompt = caption_template.render([caption, disease, knowledge, loc_descs])

```

Figure 14: Prompt used to generate multigranular annotations of multigranular textual descriptions.